Origin of bias-independent conductance plateaus and zero-bias conductance peaks in $Bi_2Se_3/NbSe_2$ hybrid structures

Hui Li,[1] Tong Zhou,[1] Jun He,[1] Huan-Wen Wang,[1] Huachen Zhang,[1] Hong-Chao Liu,[1] Ya Yi,[1] Changming Wu,[1] Kam Tuen Law,[1,*] Hongtao He,[2,†] and Jiannong Wang[1,‡]

[1]*Department of Physics, the Hong Kong University of Science and Technology, Clear Water Bay, Hong Kong, China*

[2]*Department of Physics, South University of Science and Technology of China, Shenzhen, Guangdong 518055, China*

(Received 26 July 2016; published 7 August 2017)

Superconducting proximity effect in topological insulator and superconductor hybrid structure has attracted intense attention in recent years in an effort to search for Majorana fermions in condensed matter systems. Here we report on the superconducting proximity effect in a $Bi_2Se_3/NbSe_2$ junction fabricated with an all-dry transfer method. Experimentally measured differential conductance spectra exhibit a bias-independent conductance plateau (BICP) in the vicinity of zero bias below 7 K and a zero-bias conductance peak (ZBCP) appears below 2 K. We show that the BICP is due to the strong superconducting proximity effect between the superconductor and the topological surface states while the ZBCP is due to the bulk states of Bi_2Se_3. Our study gives direct evidence that the topological surface states can be strongly coupled to a superconductor and clarifies the different roles of surface states and bulk states in superconducting proximity effect.

DOI: 10.1103/PhysRevB.96.075107

I. INTRODUCTION

Majorana fermions are long-sought fundamental particles, whose antiparticles are identical to themselves [1]. In condensed matter systems, Majorana fermions follow non-Abelian statistics and have great potential applications in fault-tolerant topological quantum computation [2,3]. Motivated by the promising applications, much effort has been devoted to the search for the signature of Majorana fermions [4–9]. Recently, theoretical work has predicted that the Majorana fermions might reside in the interface of the topological insulators and s-wave superconductors heterostructures [10–14], when superconducting vortices are created. But the basic assumption is that the topological surface states must acquire a superconducting gap from the parent superconductor to become an effective two-dimensional $p_x + ip_y$ wave superconductor residing on the surface of the topological insulator [10,11]. While many experiments have been performed on topological insulator and superconductor heterostructures [15–20], there is no clear experimental evidence that the topological surface states acquire a proximity gap from the superconductor as the observed proximity gap could be due to bulk states of the topological insulators instead of the surface states. Moreover, it is generally believed that the induced proximity gap on the topological surface states should be smaller than the superconducting gap of the parent superconductor due to surface barrier and momentum mismatch etc. [21–23].

In this paper, by studying the four-terminal differential conductance of a $Bi_2Se_3/NbSe_2$ heterostructure, we provide experimental evidence that $NbSe_2$ can induce a proximity gap almost as large as the bulk superconducting gap on the surface state. Particularly, a bias-independent conductance plateau (BICP) is observed in the differential conductance below 7 K. Judging from the width of the BICP and theoretical calculations, the proximity gap induced on the surface states is about 70% of the parent superconducting gap of $NbSe_2$.

When the temperature is lowered to below 2 K, a zero-bias conductance peak (ZBCP) emerges. We attribute this ZBCP to the Andreev reflections caused by proximity effects of the bulk states of the topological insulator. We estimated that the induced bulk proximity gap in Bi_2Se_3 is much smaller than the induced proximity gap on the surface states. The observed ZBCP is in sharp contrast to the ZBCPs observed in other superconducting topological systems in which the ZBCP were associated with surface Majorana modes.

We believe that this paper provides strong experimental evidence that the topological surface states may acquire a large proximity gap from the parent superconductor for the realization of Majorana fermions. It also clarifies the different roles of surface states and bulk states in superconducting effects in topological insulator/superconductor heterostructures.

II. EXPERIMENTAL METHODS AND RESULTS

$Bi_2Se_3/NbSe_2$ heterostructures were fabricated based on an all-dry transfer method [24]. The $NbSe_2$ flakes and Bi_2Se_3 flakes were mechanically exfoliated from the high-quality single crystals and were transferred to Si substrates with a 300-nm-thick SiO_2 and PDMS-based gel supplier, respectively. Using a micromanipulator and digital camera, the Bi_2Se_3 flakes were further transferred onto the selected $NbSe_2$ flakes for device fabrication using e-beam lithography. Au/Cr electrodes with the thickness of 275 nm/25 nm were deposited via thermal evaporation.

The optical image of a fabricated device was illustrated in Fig. 1(a). The overlap areas of the Bi_2Se_3 flake and $NbSe_2$ flake is marked as the purple dash box, with the width and the length of about 2 μm and 13 μm, respectively. The thickness of the $NbSe_2$ flake and the Bi_2Se_3 flake is confirmed by the atomic force microscope measurements, which is about 110 nm and 60 nm, respectively. A four terminal measurement across the $Bi_2Se_3/NbSe_2$ junction was performed in a PPMS Dilution

*phlaw@ust.hk
†heht@sustc.edu.cn
‡phjwang@ust.hk

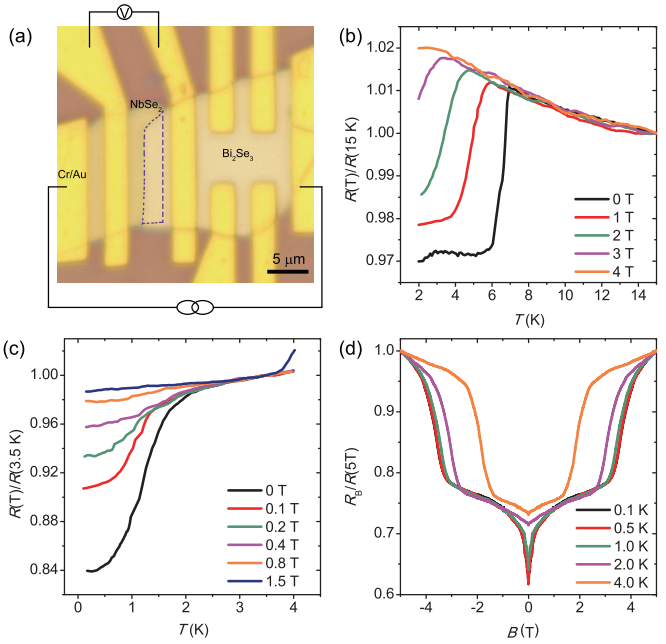

FIG. 1. $Bi_2Se_3/NbSe_2$ hybrid structure device and magnetotransport characteristics. (a) Optical image of the $Bi_2Se_3/NbSe_2$ hybrid structure devices. The purple box indicates the overlap area of the Bi_2Se_3 flake and $NbSe_2$ flake.(b) Normalized resistance-temperature curves of the $Bi_2Se_3/NbSe_2$ hybrid structures at different applied magnetic fields above 2 K; the resistance is normalized to a normal-state value at 15 K of about 40 Ω and (c) between 100 mK and 4 K, the resistance is normalized to a normal-state value at 3.5 K of about 8 Ω, showing the superconducting phase transition of $NbSe_2$ and superconducting proximity effect induced superconductivity in Bi_2Se_3. (d) Normalized resistance-magnetic field curves of the $Bi_2Se_3/NbSe_2$ hybrid structures measured at various temperatures; the resistance is normalized to a normal-state value at 5 T of about 40 Ω.

Refrigerator system with the temperature down to 100 mK. The resistance versus temperature (R-T) curves were measured using Keithley 6221 and 2182A as the current source and voltmeter, respectively. Keithley 6221 and lock-in amplifiers with a frequency of 741 Hz were adopted for the differential conductance, dI/dV, spectra measurements.

Prior to putting the devices into the PPMS dilution refrigerator, we first measured the R-T curves with $T > 2$ K in the PPMS base chamber at different magnetic fields indicated, as shown in Fig. 1(b). The resistance of the $Bi_2Se_3/NbSe_2$ junction first increases as temperature decreases and suddenly drops at a critical temperature $T_c \sim 7$ K, corresponding to the superconducting phase transition of the $NbSe_2$ flake. As the applied magnetic field increases, the T_c decreases from ∼7 K at zero magnetic field to temperatures lower than 2 K at 4 T. Interestingly, besides this sharp drop of the resistance at $T_c \sim 7$ K, a second resistance drop starts to appear below 3 K at zero magnetic field, which is attributed to the proximity-induced superconductivity in the topological insulator Bi_2Se_3 flake. The observation of superconducting proximity effects induced superconductivity in the hybrid structure suggests that the interface is of high transparency in our devices [19].

In order to investigate in details the proximity effect induced superconductivity in Bi_2Se_3 flake, we focus on the magnetotransport properties and differential conductance spectra of the $Bi_2Se_3/NbSe_2$ junction at low temperatures ranging from 0.1 K to 4 K. Figure 1(c) shows the measured R-T curves for 0.1 K $< T <$ 4 K at different magnetic fields with resistances normalized to the values at $T = 3.5$ K. At zero magnetic field, with decreasing temperature the resistance decreases slowly first and then starts to drop quickly below ∼2 K. $T_{in} \sim 2$ K corresponds to the transition temperature of the proximity-induced superconductivity in Bi_2Se_3 flake. The ratio of $R(0.1\text{ K})/R(3.5\text{ K})$ is about 0.84 at zero magnetic field. By applying magnetic fields this ratio increases to 0.97 at 1.5 T, and T_{in} shifts to lower temperatures as expected.

Magnetoresistance (MR) of the junction at different temperatures is shown in Fig. 1(d). Two important MR features are noticed at the lowest T of 0.1 K, one forming a sharp MR dip at low magnetic field region and the other forming a broader resistance valley at high magnetic field region, revealing the two critical magnetic fields for the superconducting phases existed in this hybrid structure. As temperature is increased, the sharp MR dip is quickly suppressed at ∼2 K, which coincides with the critical temperature T_{in} of the Bi_2Se_3 flake observed in R-T curves shown in Fig. 1(c). At the same time, the broad resistance valley shrinks significantly from ∼5 T at 0.1 K to ∼2 T at 4 K, which is consistent with the superconductivity transition of $NbSe_2$ flake observed in R-T curves shown in Fig. 1(b). The upper critical field H_{c2} at given T was estimated as detailed in Appendix A. The H_{c2}^{I} and H_{c2}^{II} at 0.1 K is about 1.08 T and 4.17 T, respectively. These results indicate the suppression of the Cooper pair formation and thus the destruction of the superconductivity at high temperatures and high magnetic fields.

The above R-T and MR results clearly demonstrate the occurrence of the superconducting proximity effect in our $Bi_2Se_3/NbSe_2$ junction. To gain more insight into the effect, we have performed the four-terminal differential conductance spectroscopy measurements of the junction. Figure 2(a) shows the measured differential conductance spectra (dI/dV vs V) at temperatures from 0.5 K to 4 K. One can see that a BICP appears in the vicinity of zero bias. As temperatures decrease below 2 K, a very sharp ZBCP is emerged and superimposed on the BICP. We will focus on the behavior of the BICP first. As shown in Fig. 2(a), the height of the flat conductance plateau changes little from 0.5 K to 4 K, but its width decreases obviously with increasing temperature. In Fig. 2(b) the width of the flat conductance plateau against measurement temperature is plotted as black solid dots and the temperature dependence of $NbSe_2$ superconducting gap based on BCS theory is plotted as a solid red line for reference. Its width at 0.5 K is estimated to be ∼2 meV, which is comparable to the superconducting gap of $NbSe_2$ flake estimated from the BCS theory $2\Delta(0) = 3.52k_BT_c \sim 2.12$ meV [25]. As temperature increases the width is reduced due to suppressed superconductivity of $NbSe_2$ flake. We note that the width reduction is faster than that expected from the BCS theory. This deviation may be caused by the anisotropy and Fermi-surface-sheet dependence of the superconducting gap of $NbSe_2$ [25,26]. Besides the strong temperature dependence, the width of the plateau also shows strong dependence on the applied

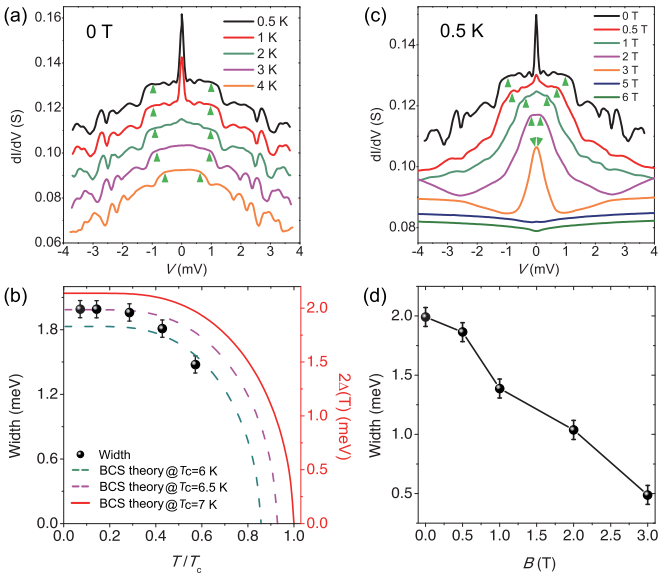

FIG. 2. Bias-independent conductance plateau (BICP) in $Bi_2Se_3/NbSe_2$ hybrid structure device. (a) Differential conductance spectra dI/dV of the $Bi_2Se_3/NbSe_2$ hybrid structures at temperatures ranging from 0.5 K to 4 K and zero magnetic field; the width of BICP is defined by the points (indicated by the green triangles) where the dI/dV starts to drop from the flat shoulder. The curves are successive offset by 0.01 S in the y direction for clarity. (b) The BICP width as a function of temperatures as indicated by black solid dots. For comparison, the temperature dependent superconducting gap of $NbSe_2$ calculated by the BCS theory with three different T_c is also plotted. (c) Differential conductance spectra dI/dV at different magnetic fields and 0.5 K; the width of BICP is defined by the points indicated by the green triangles. The curves are successive offset by 0.002 S in the y direction for clarity. (d) The BICP width as a function of magnetic field at 0.5 K is shown as black solid dots, and the solid line is a guide to the eyes.

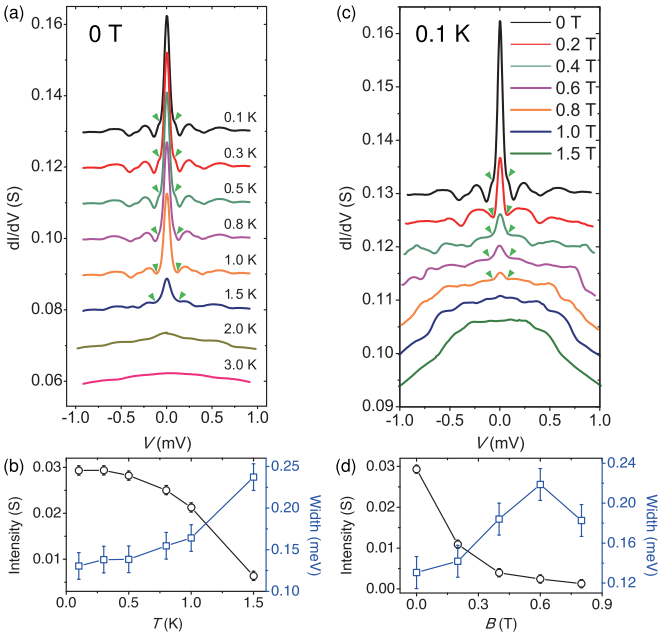

FIG. 3. Zero-bias conductance peak (ZBCP) in $Bi_2Se_3/NbSe_2$ hybrid structure device. (a) Differential conductance spectra dI/dV of the $Bi_2Se_3/NbSe_2$ hybrid structures at temperatures ranging from 0.1 K to 3 K and zero magnetic field; the width of ZBCP is defined by points indicated by the green triangles. The curves are successive offset by 0.01 S in the y direction for clarity. (b) The ZBCP peak intensity (black open circles) and width (blue open squares) as a function of temperatures at zero magnetic field. Solid lines are guides to the eyes. (c) Differential conductance spectra dI/dV at different magnetic fields and 0.1 K; the width of ZBCP is defined by points indicated by the green triangles. The curves are successive offset by 0.002 S in the y direction for clarity. (d) The peak intensity (black open circles) and width (blue open squares) as a function of magnetic field at 0.1 K. Solid lines are guides to the eyes.

magnetic field. Figure 2(c) shows the dI/dV spectra at different magnetic fields with a constant temperature of 0.5 K. It is clear that the plateau width is greatly reduced by increasing magnetic field [see Fig. 2(d)] and completely suppressed at ~5 T, in agreement with the critical magnetic field of $NbSe_2$ flake measured in Fig. 1(d).

Generally speaking, Andreev reflection is expected to greatly enhance the conductance across a normal metal and superconductor junction with an electrically transparent interface. A BICP within the superconducting gap Δ would be thus observed around zero voltage bias in the differential conductance spectra [27–29]. The evident BICP shown in Fig. 2(a) indicates that an electrical transparent interface has been achieved in our $Bi_2Se_3/NbSe_2$ device. The calculated energy difference between the Fermi level and the Dirac point is about 270 meV (see Appendix B), which is consistent with the ARPES observations on Bi_2Se_3 [30,31], indicating the Fermi level lies close to the bottom of the conduction band of the Bi_2Se_3. Since the Fermi level of our Bi_2Se_3 flake lies in the conduction band, either TSS or bulk electrons can be responsible for the BICP. As the wave function of TSS electrons is more localized at the interface than that of bulk electrons, it is very likely that superconducting transition by proximity effect occurs first in TSS once $NbSe_2$ flake becomes superconducting. Indeed, in our detailed numerical results presented in Fig. 4 (see Appendix C for details), we show that the BICP is solely due to the superconducting TSS and the proximity gap induced on the TSS by the $NbSe_2$ is almost 70% of the superconducting gap in $NbSe_2$.

We now turn the attention to the ZBCP emerged below 2 K. Figure 3(a) shows the measured differential conductance spectra at different temperatures within a smaller bias range of ± 1 mV. The ZBCP is pronounced at 1.5 K and becomes stronger and sharper as temperature decreases. The emergence of the ZBCP coincides with the second resistance drop observed in R-T curves [see Figs. 1(b) and 1(c)]. This means the ZBCP is associated with the proximity-induced superconductivity in Bi_2Se_3 flake. The temperature dependence of the ZBCP intensity and width (as defined in Appendix D) is plotted in Fig. 3(b). As it can be seen, the ZBCP intensity is first reduced slowly as temperature increases from 0.1 K to 0.5 K, then faster as temperature further increases, and finally is immeasurable around 2 K. More interestingly, the ZBCP width is almost constant below 0.5 K, which has a value of about 0.13 meV about 10% of $2\Delta(0)$ and then is quickly broadened above 1 K, which qualitatively agrees with our numerical simulation results (see Appendix E). Such behaviors are in sharp contrast to the case of the BICP [see Fig. 2(b)], where

the height changes little but the width decreases obviously with increasing temperatures. This indicates that the ZBCP width is associated with thermal energy and the energy magnitude involved in the ZBCP is at the same order as the thermal energy. For any realistic system, the finite temperature would make the Andreev reflections decoherent over a short length and thus the short lifetime. Considering the Heisenbergs uncertainty principle, $\Delta E \Delta \tau \sim \hbar$, the effective energy broadening term would be induced leading to the overall broadening of the conductance spectrum for the ZBCP [32,33]. The magnetic field dependence of the ZBCP at 0.1 K is illustrated in Fig. 3(c). With increasing applied magnetic field, the width of the ZBCP is broadened and the intensity is reduced. Figure 3(d) plots the magnetic field dependence of the ZBCP intensity and width. The ZBCP intensity decreases with the applied magnetic field. When the magnetic field is above 1 T, the ZBCP cannot be measured, in agreement with the critical magnetic field of Bi_2Se_3 flake measured in Fig. 1(d).

The ZBCP has been reported in various superconductor-normal metal hybrid structures [15,20,34–38], but its physical origin is still under debate. The ZBCP can be induced by the pair current across superconductor-semiconductor interfaces [39]. But the ZBCP width is expected to increase with decreasing temperatures, which is contrary to the thermal broadening behavior observed in our experiment. The ZBCP can also arise from the incoherent accumulation of Andreev reflection, and it begins to appear in the differential conductance spectra right below T_c [40]. However, the ZBCP in our devices can only be observed below 2 K, which is much lower than T_c. Furthermore, the Andreev bound state of an anisotropy superconductor [28,41–43] or the Majorana zero mode in the core of the vortices of topological superconductor [12,44] can also give rise to the ZBCP. ZBCPs of these kinds usually show a weak dependence on the magnetic field. However, these are apparently not our case. The ZBCP observed is quenched quickly by small external magnetic field [see Fig. 3(c)].

In addition, we note that some differential conductance ripples appear outside the BICP in Fig. 2(a) and the ZBCP in Fig. 3(a). Similar ripples were observed in differential conductance spectra outside the superconducting gap region in the study of an Al-Al_2O_3-Pb tunneling junction [45]. The phenomenon was ascribed to the multiphonon effect, revealing the important role of phonon interactions in the superconductivity of Pb. Besides, in the study of UPd_2Al_3-AlO_x-Pb tunneling junctions, the observation of such ripples was associated with some magnetic excitations, which is essential to the emergence of unconventional superconductivity in heavy fermion compound UPd_2Al_3 [46]. At the present stage, the physical origin of the ripples observed in our work is still unknown and needs further exploration. But these ripples show the same temperature and magnetic field dependence as the BICP or the ZBCP, indicating the close relationship between the ripples and the SPE induced superconductivity in TSS or bulk states of Bi_2Se_3.

III. ORIGINS OF THE BICP AND ZBCP

To summarize the experimentally measured differential conductance spectra at low temperature and zero magnetic field exhibit two distinct features: One is the sharp ZBCP with its width approximately 10% of $2\Delta(0)$ and the other is the BICP with its energy range comparable to $2\Delta(0)$. In order to understand the physical origins of both the ZBCP and the BICP, we theoretically calculate the dI/dV spectra for our $Bi_2Se_3/NbSe_2$ junction. In our theoretical calculations (see Appendix C for details), we simulate the $Bi_2Se_3/NbSe_2$ junction with the schematic set-up in Fig. 4(a), which realistically represents our device structure, where the chemical potential of the TI is just touching the bulk conduction band bottom [e.g., $E_F = \mu_1$, indicated by the red dashed line in the inset of Fig. 4(b)]. The $\mu_1 = 274$ meV is used in our numerous calculation, which is consistent with our experimental observations and the previous ARPES studies on Bi_2Se_3 [30,31]. In this case, the Fermi surface consists of multiple Fermi circles, where the outermost Fermi circle derived from the TSS encloses the inner one derived from the bulk states. Therefore, both the bulk states and the TSS from Bi_2Se_3 would participate in the proximity effects and drive currents across the $Bi_2Se_3/NbSe_2$ junction via Andreev reflections.

The dI/dV spectra from our numerical simulations with $E_F = \mu_1$ is shown in Fig. 4(b). Remarkably, both features of BICP and ZBCP are reproduced in a qualitatively excellent agreement with the experimental data [see Figs. 2(a) and 3(a)]. More importantly, by increasing the number of quintuple layers N of Bi_2Se_3, the sharp ZBCP is enhanced, while the BICP remains almost unaffected. Their contrasting dependence on N suggests that the ZBCP may be associated with the bulk states near the conduction band minimum, while the BICP likely originates from the TSS. For each fixed momentum k (assuming momentum is conserved parallel to the surface), there is only one mode from the surface states to contribute to Andreev reflection processes. However, for each momentum k, there are a large number of modes in the bulk to involve in Andreev reflections. Therefore, as shown in Fig. 4(b), the height of the peak indeed depends on the number of quintuple layers. The larger the number of layers, the larger the number of bulk states at each fixed k which induces a higher ZBCP. Therefore, within the energy window in which the bulk states can induce Andreev reflections, the ZBCP can be quite high as shown in our numerical calculations and experimental observations. When the magnetic field is applied, the proximity induced superconductivity in the bulk states of Bi_2Se_3 is gradually suppressed, and the height of the ZBCP decreases. As the magnetic field exceeds 1 T, the proximity effect in the bulk states of the Bi_2Se_3 is destroyed. As a result, the ZBCP vanishes [Fig. 3(c)], and the second resistance drop around 2 K also disappears [Fig. 1(c)].

To further verify the physical origins of the peak and the plateau, we calculate the dI/dV spectra for our $Bi_2Se_3/NbSe_2$ junction in another two separate cases. First, we study the case where only the TSS in Bi_2Se_3 is involved in the proximity effect. By setting the chemical potential in Bi_2Se_3 to lie within the bulk gap [$E_F = \mu_2$ indicated by the green dashed line in the inset of Fig. 4(c)], we exclude the contributions from the bulk states and the Andreev reflections at low-voltage bias are driven by the TSS only. As shown in Fig. 4(c), the ZBCP vanishes, while the BICP remains intact and its height is almost unchanged with the quintuple-layer number N. Therefore, we confirm that the BICP indeed originates from the proximity

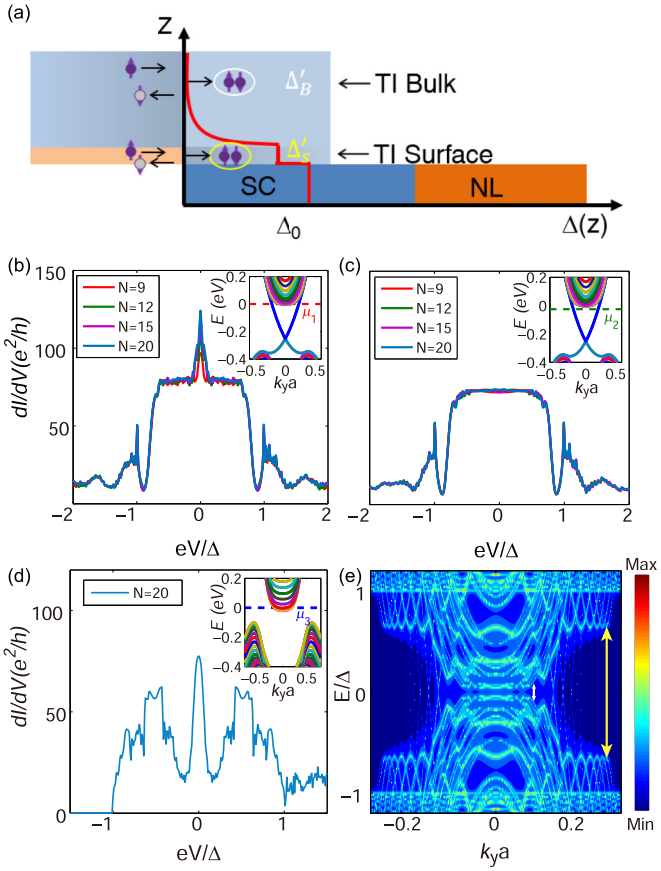

FIG. 4. Numerical simulations of the differential conductance spectra dI/dV and the superconducting proximity effect for the $Bi_2Se_3/NbSe_2$ hybrid structure. The insets in (b)–(d) show the energy spectrum of Bi_2Se_3 near the Γ point with $k_x = 0$ in the surface Brillouin zone. The dashed lines indicate the locations of the Fermi energy in each individual case. (a) Schematic showing the Andreev reflections and the superconducting proximity effect in the topological insulator/superconductor junction. (b),(c) Zero-temperature dI/dV spectra for topologically nontrivial Bi_2Se_3 with different numbers of quintuple layers $N = 9$, 12, 15, 20. The Fermi energy of Bi_2Se_3 in (b) is set to be $E_F = \mu_1$ (see inset) such that both the surface states and the bulk states near the conduction band minimum are filled. Both features of the zero-bias conductance peak and bias-independent conductance plateau are reproduced in qualitatively good agreement with the experimental data. The Fermi energy of Bi_2Se_3 in (c) is set to be $E_F = \mu_2$ (see inset) such that only the surface states are filled. The zero-bias conductance peak disappears while the flat plateau remains almost unaffected by the number of quintuple layers N. (d) Zero-temperature dI/dV spectra for topologically trivial Bi_2Se_3 with $N = 20$. The Fermi energy of Bi_2Se_3 is set to be $E_F = \mu_3$ (see inset) such that only the bulk conduction band minimum is filled. The zero-bias conductance peak remains while the bias-independent conductance plateau disappears. (e) The spectral weight of the bottom quintuple layer of a section of TI placed right on top of superconducting $NbSe_2$ thin flakes. The Fermi energy of Bi_2Se_3 is the same as in (b). The double arrows in yellow/white indicate twice the induced gaps $2\Delta'_S/2\Delta'_B$ on the surface/bulk states. Evidently, Δ'_S is significantly greater than Δ'_B.

effect in the TSS. Second, we study the case where only the bulk states near the conduction band bottom of Bi_2Se_3 are filled at the Fermi energy. This is done by tuning the tight-binding parameters of Bi_2Se_3 such that it becomes a trivial band insulator with $E_F = \mu_3$ as shown in the inset of Fig. 4(d) indicated by the blue dashed line. In this case, the BICP disappears in the dI/dV spectra with only a sharp ZBCP left [Fig. 4(d)], confirming that the sharp ZBCP arises from the proximity effect in the bulk states near the conduction band bottom.

Their contrasting signatures in the dI/dV spectra suggest that the bulk states and surface states in Bi_2Se_3 behave very differently in the superconducting proximity effect. To understand their distinct roles in the proximity effect, we calculate the spectral function of Bi_2Se_3 with $E_F = \mu_1$ placed right on top of superconducting $NbSe_2$, as shown in Fig. 4(e). Evidently, the outermost Fermi circle associated with the TSS acquires a sizable induced gap Δ'_S [$2\Delta'_S$ is indicated by the double arrow in yellow in Fig. 4(e)] that is about 70% compared to the parent superconducting gap Δ. This result is consistent with the experimentally obtained width of the BICP at low temperature [see Fig. 2(b)]. In contrast, the induced gaps on the inner Fermi circles Δ'_B [$2\Delta'_B$ is indicated by the double arrow in white in Fig. 4(e)] are an order of magnitude smaller in size, which is also in agreement with the experimentally obtained ZBCP width [see Fig. 3(b)]. In other words, the proximity effect in the TSS are much stronger compared to that in the bulk states. The strong proximity effect and large induced gap in the TSS give rise to the BICP observed in our experiment at temperatures a bit below the host T_c [see Fig. 2(b) dashed curves, estimated as 6.5 K]. On the other hand, the weak proximity effect and small induced gap in the bulk states are responsible for the ZBCP observed below 2 K, which is much lower than the host T_c. In brief, the BICP is a result of Andreev reflection driven by the surface states through a very transparent interface between the topological insulator Bi_2Se_3 and the superconductor, corresponding to the $Z \approx 0$ case with Z being the interface barrier strength in the Blonder-Tinkham-Klapwijk (BTK) theory [27]. The ZBCP is due to the Andreev reflections driven by the bulk states of Bi_2Se_3 for energies lower than the small proximity induced gap Δ'_B.

To understand the different proximity gaps induced in the surface states and that on the bulk states, we note that the wave functions of the surface states are localized at the surface, while wave functions of the bulk states are predominantly in the bulk. Effectively, the surface states couple much more strongly to the superconductor than the bulk states. Consequently, the proximity-induced gap on the surface states is much larger than that in the bulk resulting in different T_c. We also note that high interfacial transparency is crucial for the observation of the flat BICP as clearly illustrated in Appendix F. The BICP can only be observed when the interface is highly transparent. When the coupling strength, or interfacial transparency, between the topological insulator and the superconductor is reduced, the width of the BICP is reduced. Further reducing the interfacial transparency will remove the BICP completely. This gives strong evidence that a highly transparent junction is achieved in the experiment. The Thouless energy of the bulk states of Bi_2Se_3 was also estimated as illustrated in Appendix G, which is about 0.036 meV, close to the ZBCP width we measured from the experimental dI/dV spectra in Fig. 3(a) [47,48].

IV. CONCLUSIONS

In conclusion, the superconducting proximity effect is investigated in $Bi_2Se_3/NbSe_2$ hybrid structure with transparent interface. Two distinct features in the measured differential conductance spectra are revealed: One is the BICP observed once $NbSe_2$ becomes superconducting and the other is the sharp ZBCP emerged at much lower temperature. Both features are reproduced in our theoretical calculations. We identify that the ZBCP originates from the proximity effect in the bulk states, while the pronounced BICP results from the proximity effect in the TSS. Our experiment provides direct evidence that the topological surface state acquires a large proximity gap from the $NbSe_2$. As a result, the effective $p_x + ip_y$ superconductor can be realized. This suggests our $Bi_2Se_3/NbSe_2$ junction can be a promising candidate for realizing Majorana fermions at the vortex core on the surface of a 3D topological insulator. Our work not only provides new insight into the different roles of TSS and bulk states in the superconducting proximity effect of topological insulators, but also proposes a new physical mechanism for ZBCP, which would have some implications to the search for Majorana fermions in topological insulator and superconductor hybrid structures.

ACKNOWLEDGMENTS

This work was supported in part by the Research Grants Council of the Hong Kong Special Administrative Region in China under Grants No. 16305215, No. AOE/P-04/08-3-II, No. HKU9/CRF/13G-1, No. HKUST3/CRF/13G, and No. C6026-16W, in part by the National Natural Science Foundation of China under Grants No. 11574129 and No. 11374135, and in part by the Special Funds for the Development of Strategic Emerging Industries of Shenzhen in China (Grant No. JCYJ20140714151402765). K. T. Law acknowledges the support of Croucher Foundation of Hong Kong. The electron-beam lithography facility is supported by the Raith-HKUST Nanotechnology Laboratory in Materials Characterization and Preparation Facility of Hong Kong University of Science and Technology.

H.L and T.Z. contributed equally to this paper.

APPENDIX A: CRITICAL FIELDS H_{c2} FOR THE SUPERCONDUCTING TRANSITION

As in ordinary superconductors, the upper critical fields can be defined as the strength of fields at which the resistance of the system is restored to the normal state value. In our system, when the magnetic field increases, the resistance increases linearly for B field from about 1 T to 3 T [fitted by the dashed line 1 in Fig. 5(a) for measurements conducted at 0.5 K] [49]. Below 1 T, the resistance is reduced below the linear regime. We expect that this reduction in resistance is due to proximity effect induced superconductivity in Bi_2Se_3. Since the resistance is restored to the weak-antilocalization regime at about 1.08 Tesla, we determine that the upper critical field for the proximity effect induced superconductivity, H_{c2}^{I}, is 1.08 Tesla. This value of H_{c2}^{I} is also consistent with the fact that the zero-bias conductance peak vanishes at around 1 Tesla in Fig. 2(c) of the paper. The vanishing of the zero-bias peak indicates that the proximity effect of the bulk states are killed by the magnetic field.

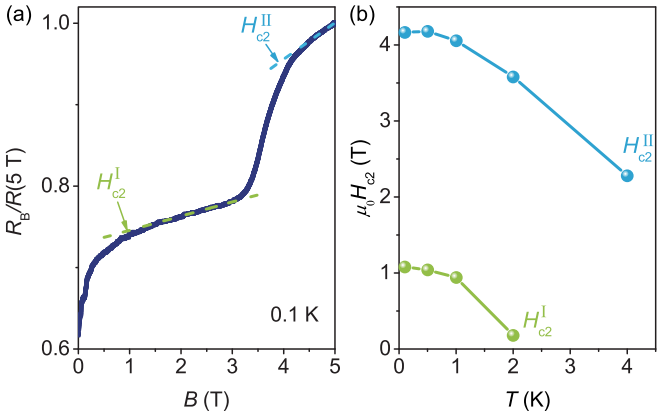

FIG. 5. Magnetoresistance measurements of upper critical fields H_{c2} in $Bi_2Se_3/NbSe_2$ hybrid structures. (a) R-H curve of $Bi_2Se_3/NbSe_2$ hybrid structures measured at 0.5 K. The determination procedure of H_{c2}^{I} and H_{c2}^{II} is indicated. (b) The upper critical fields H_{c2}^{I} and H_{c2}^{II} as a function of T.

As the magnetic field keeps increasing up to 4.17 Tesla, the normal state resistance for the junction is restored (fitted by the dashed line 2). Therefore, we determine that the H_{c2} for the $NbSe_2$ thin film, H_{c2}^{II}, is 4.17 Tesla. This value of H_{c2}^{II} is very reasonable as the H_{c2} for bulk $NbSe_2$ is about 5 Tesla (for magnetic field perpendicular to the $NbSe_2$ planes) [50]. The upper critical fields, H_{c2}^{I} and H_{c2}^{II}, as a function of temperature are plotted in Fig. 5(b).

APPENDIX B: MAGNETORESISTANCE PROPERTIES OF n-Bi_2Se_3 FLAKES

For comparisons, the magnetoresistance properties of the n-Bi_2Se_3 flakes exfoliated onto SiO_2 (290 nm)/Si substrates from the same piece of n-Bi_2Se_3 bulk crystals supplied by the 2D Semiconductor Company were also investigated. Figure 6(a) shows the magnetoresistances of the n-Bi_2Se_3 flakes measured at 3 K with magnetic fields perpendicular with the planes of the n-Bi_2Se_3 flakes, namely $\theta = 0^o$, where θ is the angle between the normal direction of the sample plane and the magnetic fields. Hall measurements confirm the n type of the Bi_2Se_3 flakes with the carrier density of $2.27 \times 10^{19}/cm^3$. The SdH oscillations superimposed on the smooth polynomial backgrounds were clearly observed at the high magnetic fields above ~7 T. To analyze the SdH oscillations, ΔR_{xx}-$1/B$ curve was plotted by removing the smooth polynomial background. As shown in Fig. 6(b), the ΔR_{xx} exhibits periodic dependence on the $1/B$ at high magnetic fields. By applying the fast Fourier transformation to the oscillations, the oscillation frequencies F was estimated to be 168.67 T, as shown in Fig. 6(c), and was almost the same with our previous reports [51].

The angle dependence of the magnetoresistance was also measured, as plotted in Fig. 7(a). It can be seen that the SdH oscillations are only dependent on the perpendicular component of the magnetic fields. When θ increases, the amplitudes of the SdH oscillations decreases as well, and the

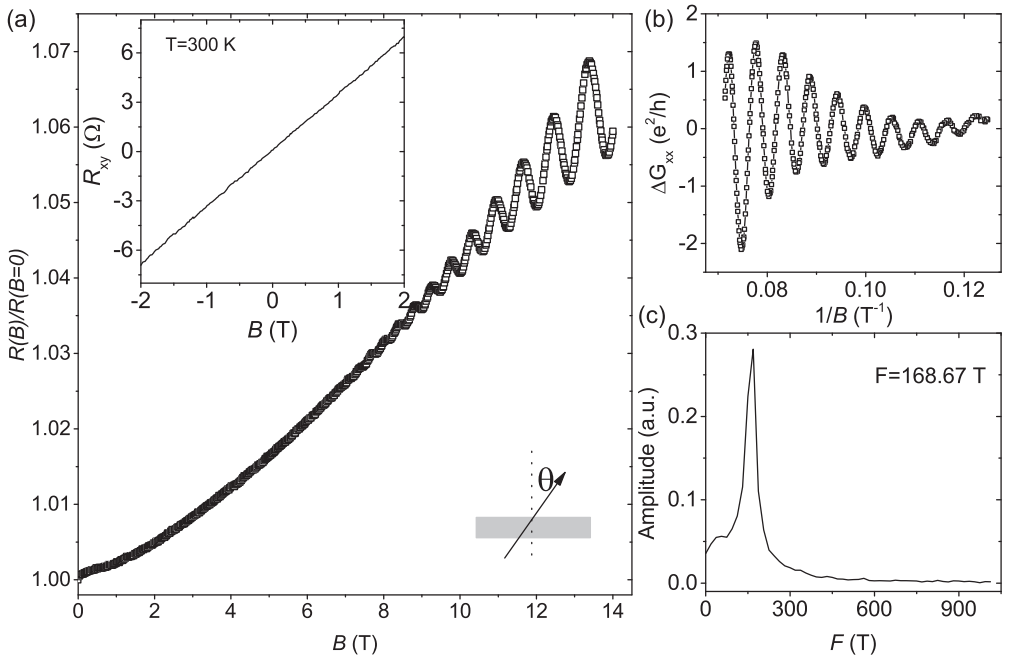

FIG. 6. Magnetoresistance and SdH oscillations of the exfoliated n-Bi_2Se_3 flakes. (a) the magnetoresistance of the n-Bi_2Se_3 flakes at 3 K, where the SdH oscillations superimposed are clearly observed. Left top inset is the Hall measurements at 300 K, while the right bottom inset is the schematic drawing of the n-Bi_2Se_3 flakes in magnetic fields with tilted angle θ. (b) The ΔR_{xx} as a function of $1/B$. (c) The oscillation frequencies calculated by fast Fourier transformation.

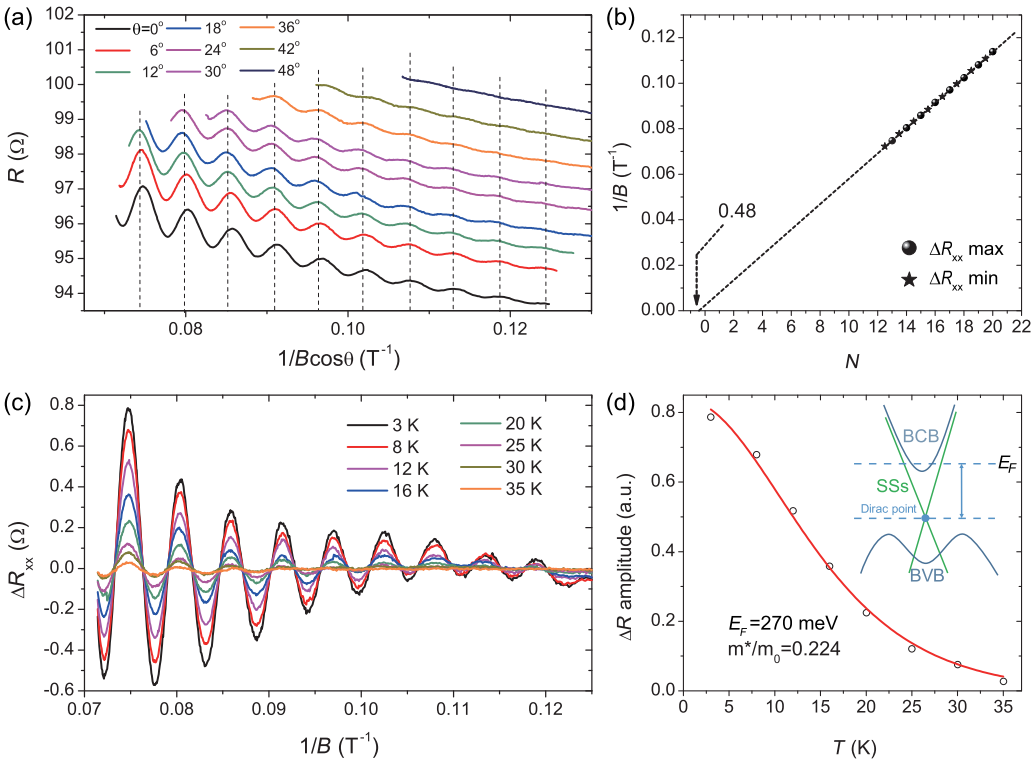

FIG. 7. SdH oscillations of the exfoliated n-Bi_2Se_3 flakes and band structure. (a) Angle dependence of the SdH oscillations at 3 K. (b) The Landau level fan diagram of n-Bi_2Se_3 flakes. The integer (n) and half integer ($n+1/2$) marked as star and circle, respectively, correspond to the maxima and minima of the conductivity ΔR_{xx}. The linear fitting (red line) gives the n-axis intercept of 0.48. (c) Temperature dependence of the SdH oscillations at $\theta = 0°$. (d) The SdH oscillation amplitude as a function of temperature; the red line is the fitting using L-K theory providing the cyclotron mass $m^* = 0.224m_0$. The inset is the schematic of the band structure based on the quantitative estimations of the SdH oscillations; the Fermi energy E_F is estimated to be about 270 meV.

SdH oscillations are hardly recognized when θ increases to about 48°. The angle dependent SdH oscillations were also reported in previous studies on topological insulators, which is due to the SdH oscillations come from the topological surface states that has the two-dimensional (2D) nature. To verify it, we plotted the Landau level fan diagrams based on the oscillations shown in Fig. 7(b). According to the standards Lifshitz-Kosevich (L-K) theory, the 2D SdH oscillations follow the equation, $\Delta R_{xx} = R(B,T)\cos[2\pi(F/B - 1/2 + \beta)]$, where $R(B,T)$ is the amplitude of the SdH oscillations, and $2\pi\beta$ is the Berry phase that is π for ideal Dirac fermions and 0 for normal electrons. The Landau level indexes with the half-integer/integer were obtained by considering the minima/maxima of the ΔR_{xx}. By linear fitting the Landau indexes, the intercept β is calculated to be about 0.48, indicating the SdH oscillations are arising from the nontrivial topological surface states.

The SdH oscillations are also systemically investigated at different temperatures at high magnetic fields, as shown in Fig. 7(c). With the temperature increases, the SdH oscillations amplitude decreases gradually. According to the L-K theory, the oscillations amplitude $R(B,T) = R_0 \frac{2\pi^2 k_B T}{(\hbar\omega_c \sinh(2\pi^2 k_B T/\hbar\omega_c)} \exp(-(2\pi^2 k_B T_D)/(\hbar\omega_c))$, where R_0 is the zero field resistance, k_B is the Boltzmann constant, $\omega_c = eB/m^*$ is the cyclotron frequency, and m^* is the cyclotron mass, $T_D = \hbar/(2\pi\tau_D k_B)$ is the Dingle temperature, and τ_D is the Dingle scattering time corresponding to dephasing of the Landau states. Based on the equation, the m^* can be estimated by fitting the temperature dependence of SdH amplitude at fixed B. As shown in Fig. 7(d), the fitting gives rise to $m^* = 0.224m_0$, where m_0 is the electron rest mass.

For Dirac fermions, the linear energy dispersion relation of the topological surface states leads to the Fermi velocity $v_F = \hbar k_F/m^*$, where $k_F^2 = 2eF/\hbar$ is given by the Onsager relation. Thus the Fermi velocity v_F is calculated as $5.92 \times 10^5 m/s$, and the energy difference between the Fermi level and the Dirac point is further estimated by considering $E = \hbar v_F k_F$, which is about 270 meV, as shown in the schematic drawing in the inset of Fig. 7(d). These quantitative estimations are consistent with the ARPES observations on Bi_2Se_3, from which the band structure is adopted in our numerical calculations [30,31].

APPENDIX C: NUMERICAL CALCULATIONS OF DIFFERENTIAL CONDUCTANCE FOR $Bi_2Se_3/NbSe_2$ JUNCTION

In this section, we present the detailed descriptions of the tight-binding model used in our numerical simulations. The total Hamiltonian for the $Bi_2Se_3/NbSe_2$ junction can be written as:

$$\mathcal{H}_{\rm tot} = \mathcal{H}_{TI} + \mathcal{H}_{SC} + \mathcal{H}_c, \tag{C1}$$

where H_{TI}/H_{SC} refer to the Hamiltonians for the 3D topological insulator Bi_2Se_3 and the $NbSe_2$ thin flakes, respectively. H_c is the coupling Hamiltonian at the topological insulator/superconductor (TI/SC) interface.

First, we model H_{TI} using the tight-binding Hamiltonian for Bi_2Se_3 in Refs. [52,53], which in the basis $\boldsymbol{c_k} = (c_{\boldsymbol{k},+\uparrow}, c_{\boldsymbol{k},+\downarrow}, c_{\boldsymbol{k},-\uparrow}, c_{\boldsymbol{k},-\downarrow})^T$ is written as:

$$\mathcal{H}_{TI} = \sum_{\boldsymbol{k}} \boldsymbol{c}_{\boldsymbol{k}}^\dagger H_{TI}(\boldsymbol{k}) \boldsymbol{c}_{\boldsymbol{k}}, \tag{C2}$$

where the $\pm$ sign refers to the spatial parity of the basis wave functions, and $\uparrow$, $\downarrow$ label the spin indices. The 4×4 matrix $H_{TI}(\boldsymbol{k})$ takes the form:

$$H_{TI}(\boldsymbol{k}) = \mathcal{E}(\boldsymbol{k}) I_{4\times 4} + \begin{pmatrix} \mathcal{M}(\boldsymbol{k}) & 0 & \mathcal{B}(\boldsymbol{k}) & \mathcal{A}_-(\boldsymbol{k}) \\ 0 & \mathcal{M}(\boldsymbol{k}) & \mathcal{A}_+(\boldsymbol{k}) & -\mathcal{B}(\boldsymbol{k}) \\ \mathcal{B}(\boldsymbol{k}) & \mathcal{A}_-(\boldsymbol{k}) & -\mathcal{M}(\boldsymbol{k}) & 0 \\ \mathcal{A}_+(\boldsymbol{k}) & -\mathcal{B}(\boldsymbol{k}) & 0 & -\mathcal{M}(\boldsymbol{k}) \end{pmatrix} \tag{C3}$$

and its matrix elements are defined as:

$$\begin{aligned} \mathcal{E}(\boldsymbol{k}) &= C_0 - E_F + 2C_1[1 - \cos(k_z c)] \\ &\quad + 2C_2[2 - \cos(k_x a) - \cos(k_y a)] \\ \mathcal{M}(\boldsymbol{k}) &= M_0 + 2M_1[1 - \cos(k_z c)] \\ &\quad + 2M_2[2 - \cos(k_x a) - \cos(k_y a)] \\ \mathcal{A}(\boldsymbol{k}) &= A_0[\sin(k_x a) + i \sin(k_y a)] \\ \mathcal{B}(\boldsymbol{k}) &= B_0 \sin(k_z c). \end{aligned}$$

Here, a refers to the lattice constants in the ab plane, and c denotes the distance between neighboring quintuple layers in Bi_2Se_3. The parameters $C_0, C_1, C_2, M_0, M_1, M_2, A_0, B_0$ are in the units of energy (eV) with their values given in Table I. E_F denotes the chemical potential of the TI.

Second, we model the superconducting $NbSe_2$ layers by a quasi-2D s-wave superconductor with square lattice geometry. In the Nambu basis $\boldsymbol{\Psi_k} = (\psi_{\boldsymbol{k},\uparrow}, \psi_{\boldsymbol{k},\downarrow}, \psi^\dagger_{-\boldsymbol{k},\uparrow}, \psi^\dagger_{-\boldsymbol{k},\downarrow})^T$, the bulk Hamiltonian for the superconductor is given by:

$$\begin{aligned} \mathcal{H}_{SC} &= \sum_{\boldsymbol{k}} \boldsymbol{\Psi}_{\boldsymbol{k}}^\dagger H_{SC}(\boldsymbol{k}) \boldsymbol{\Psi_k} \\ H_{SC}(\boldsymbol{k}) &= [2t(\cos(k_x a) + \cos(k_y a) + \cos(k_z a)) \\ &\quad - \mu_s]\sigma_0\tau_z + \Delta\sigma_y\tau_y. \end{aligned} \tag{C4}$$

Here, t, μ_s, Δ refer to the hopping amplitude, the chemical potential, and the mean-field order parameter of the superconductor.

Third, to simulate the TI/SC junction, we introduce the coupling Hamiltonian H_c at the TI/SC interface. In our transport experiment, the junction is formed with a section of Bi_2Se_3 placed right on top of superconducting $NbSe_2$ thin films [Fig. 1(a) of the main text]. For a realistic simulation of the experimental junction, the coupling Hamiltonian H_c

TABLE I. Parameters for the Hamiltonian $H_{\rm tot}$. All the parameters are set in units of eV.

C_0	C_1	C_2	M_0	M_1	M_2	A_0	B_0	μ_1	t	Δ	μ_s	t_c
−0.0083	0.024	1.77	−0.28	0.216	2.60	0.80	0.32	0.274	−0.20	0.02	−1.0	−0.20

at the TI/superconductor interface is modeled by hopping matrices which connect a section of the Bi_2Se_3 bottom surface to the sites right below on the top surface of the superconductor.

As shown in Fig. 4(a), once the TI/SC junction is formed, translational symmetries in the x,z directions are broken. Therefore, we use the real-space Hamiltonian derived from $H_{TI}(\boldsymbol{k})$ and $H_{SC}(\boldsymbol{k})$ with open boundary conditions in x/z directions. Assuming translational invariance in the y direction, we can still treat k_y as a good quantum number and the separate parts of the Hamiltonian—$\mathcal{H}_{TI}$, $\mathcal{H}_{SC}$, and $\mathcal{H}_c$—can be written in block-diagonal form as:

$$\mathcal{H}_{TI}=\sum_{k_y}\mathcal{H}_0(k_y)\quad \mathcal{H}_{SC}=\sum_{k_y}\mathcal{H}_s(k_y)\quad \mathcal{H}_c=\sum_{k_y}\mathcal{H}_c(k_y), \tag{C5}$$

where for each fixed k_y we have:

$$\begin{aligned}\mathcal{H}_0(k_y)=&\sum_{m=1}^{N_x}\sum_{n=1}^{N_z}\sum_{ss',\sigma\sigma'}c^{\dagger}_{mn,s\sigma}(k_y)[H_{TI,mn}(k_y)]_{s\sigma,s'\sigma'}c_{mn,s'\sigma'}(k_y)\\&+\sum_{m=1}^{N_x}\sum_{n=1}^{N_z-1}\sum_{ss',\sigma\sigma'}c^{\dagger}_{(m,n+1),s\sigma}(k_y)[H_z(k_y)]_{ss',\sigma\sigma'}c_{(m,n),s'\sigma'}(k_y)+\text{H.c.}\\&+\sum_{m=1}^{N_x-1}\sum_{n=1}^{N_z}\sum_{ss',\sigma\sigma'}c^{\dagger}_{(m+1,n),s\sigma}(k_y)[H_x(k_y)]_{ss',\sigma\sigma'}c_{(m,n),s'\sigma'}(k_y)+\text{H.c.}\end{aligned} \tag{C6}$$

Here, (m,n) labels the lattice vectors $\boldsymbol{R}=ma\hat{x}+nc\hat{z}$ of the 3D TI in the xz plane and s/σ are the parity/spin indices, respectively. The matrices $H_{x/z}$ are the hopping matrices along the directions defined by unit vectors $\hat{x}/\hat{z}$, which are obtained from $H_{TI}(\boldsymbol{k})$ by partial Fourier transforms. Similarly, for the quasi-2D superconductor we have:

$$\begin{aligned}\mathcal{H}_s(k_y)=&\sum_{l=1}^{N_x'}\sum_{p=1}^{N_z'}\psi^{\dagger}_{lp,\sigma}(k_y)[2t\cos(k_ya)-\mu_s]\psi_{lp,\sigma}(k_y)\\&+[\Delta\psi^{\dagger}_{lp,\uparrow}(k_y)\psi^{\dagger}_{lp,\downarrow}(-k_y)+\text{H.c.}]\\&+\sum_{l=1}^{N_x'}\sum_{p=1}^{N_z'-1}\sum_{\sigma}t(\psi^{\dagger}_{(l,p+1),\sigma}\psi_{(l,p),\sigma}+\text{H.c.})\\&+\sum_{l=1}^{N_x'-1}\sum_{p=1}^{N_z'}\sum_{\sigma}t(\psi^{\dagger}_{(l+1,p),\sigma}\psi_{(l,p),\sigma}+\text{H.c.}).\end{aligned} \tag{C7}$$

Here, (l,p) labels the lattice vectors $\boldsymbol{R'}=la\hat{x}+pa\hat{z}$ of the superconductor in the xz plane. By assuming the TI and the superconductor are coupled at the interface by hopping terms that preserve spins σ and momenta k_y, we have:

$$\begin{aligned}\mathcal{H}_c(k_y)=&\sum_{\langle\boldsymbol{R},\boldsymbol{R'}\rangle,s\sigma}t_c\psi^{\dagger}_{\boldsymbol{R'},\sigma}(k_y)c_{\boldsymbol{R},s\sigma}(k_y)+\text{H.c.}\\=&\sum_{m,s,\sigma}t_c\psi^{\dagger}_{(m,N_z'),\sigma}(k_y)c_{(m,1),s\sigma}(k_y)+\text{H.c.},\end{aligned} \tag{C8}$$

where $m\in$ interface.

In our simulations for the differential conductance $G_c=dI/dV$ measured in the experimental setup, we consider a semi-infinite Bi_2Se_3 with a small section of its bottom layer attached to the top layer of the superconductor as shown in Fig. 4(a) in the main text. On the other end of the superconductor, we also attach a semi-infinite lead which has the same lattice geometry as the superconductor and is modeled by the same tight-binding parameters as in $\mathcal{H}_{SC}$ except $\Delta=0$. With the model Hamiltonians H_{TI},H_{SC},H_c above, the dI/dV spectra for our TI/SC junction can be calculated using the scattering matrix approach:

$$G_c(E)=\frac{e^2}{h}Tr\{I\sigma_0-r_{ee}(E)^{\dagger}r_{ee}(E)+r^{\dagger}_{he}(E)r_{he}(E)\}, \tag{C9}$$

where r_{ee}, r_{he} refer to the scattering matrices for normal/Andreev reflections, respectively. By current conservation law, the same value of $G_c(E)$ can be obtained from scattering matrices defined at any interface in the semi-infinite Bi_2Se_3. To calculate the scattering matrix in a convenient way, we choose the interface between the semi-infinite Bi_2Se_3 and the section of Bi_2Se_3 on top of the s-wave superconductor as shown schematically in Fig. 4(a) in the main text.

Due to translational invariance in the y direction, the total scattering matrix can be brought into block-diagonal form, with each sub-block characterized by a momentum k_y. Using the recursive Greens function method [54], the sub-block for a fixed k_y is obtained as:

$$r_{\alpha\beta}(E,k_y)=-I\sigma_0\delta_{\alpha\beta}+i\Gamma^{1/2}_{\alpha}(E,k_y)G^R_{ii}(E,k_y)\Gamma^{1/2}_{\beta}(E,k_y). \tag{C10}$$

Here, $\alpha,\beta\in\{e,h\}$ are the electron/hole indices, σ_0 is the identity matrix in the spin space, and I is the identity matrix in the rest of the Hilbert space. $G^R_{ii}(E,k_y)=[E+i\eta-H_{\text{tot}}(k_y)]^{-1}_{ii}$ is the retarded Greens function at the interface between the semi-infinite Bi_2Se_3 and the $Bi_2Se_3/NbSe_2$ junction. Γ is the broadening function defined as $\Gamma(E,k_y)=i[\Sigma(E,k_y)-\Sigma^{\dagger}(E,k_y)]$, where $\Sigma(E,k_y)$ is the self-energy of the semi-infinite Bi_2Se_3. The total differential conductance is obtained

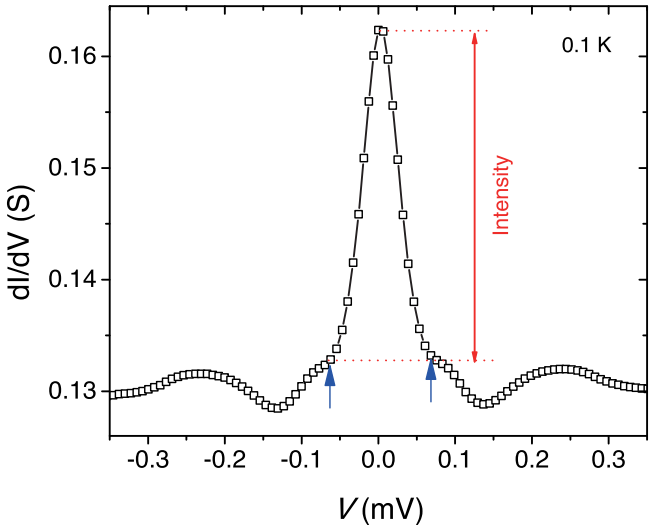

FIG. 8. Estimation of the width for the ZBCP at 0.1 K of the $NbSe_2/Bi_2Se_3$ hybrid structures. The width was determined by the bias positions of the inflection points, as indicated by the blue arrows. The red double-headed arrow represents the intensity of the ZBCP.

by summing the traces of all sub-blocks:

$$G_c(E) = \frac{e^2}{h}\sum_{k_y} Tr\{I\sigma_0 - r_{ee}(E)^\dagger r_{ee}(E) + r_{he}^\dagger(E) r_{he}(E)\}. \tag{C11}$$

APPENDIX D: ESTIMATION OF THE WIDTH AND INTENSITY OF THE ZBCP

The width of ZBCP in Fig. 3 in the main text was determined by the bias positions of the inflection points, as indicated by the blue arrows shown in Fig. 8, while the ZBCP intensity is determined by the peak conductance value relative to the inflection point, as indicated by the red double-headed arrow.

APPENDIX E: THEORETICALLY MODELING THE TEMPERATURE DEPENDENCE OF ZERO-BIAS CONDUCTANCE PEAKS

In this section, we demonstrate the thermal smearing effects on zero-bias conductance peaks (ZBCPs) based on the differential current formula derived in Ref. [55]. The conductance formula under finite temperature is given by [55]:

$$G_c(E,T) = \frac{e^2}{h}\int dE' Tr[I - r_{ee}^\dagger(E') r_{ee}(E') + r_{he}^\dagger(E') r_{he}(E')] \times \left[-\frac{\partial f_{FD}(E',T)}{\partial E'}\right]. \tag{E1}$$

Here, the scattering matrices r_{ee}, r_{he} are defined as Eq. (C9) in Appendix C. $f_{FD}(E,T) = 1/[\exp(\frac{E}{k_B T} + 1]$ is the Fermi-Dirac distribution function.

In general, thermal fluctuations have two major effects on ZBCPs: One is the reduction of peak intensity, and the other is the broadening of the peak width. These two effects are demonstrated in Fig. 9(a) by calculating the dI/dV spectra under finite-temperature conditions. The dimensionless

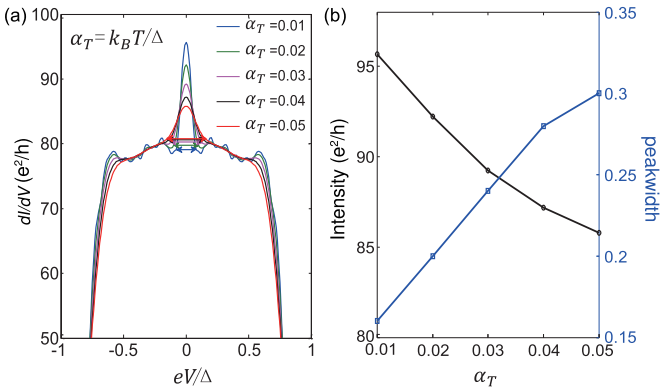

FIG. 9. Numerical simulation of the dI/dV spectra at different α_T, where α_T denotes the ratio between the thermal energy $k_B T$ and the pairing gap Δ. (a) The dI/dV spectra at different α_T. (b) The peak intensity and peak width as a function of α_T. By increasing α_T, the peak intensity is reduced, while the peak width is broadened.

parameter α_T denotes the ratio between the thermal energy $k_B T$ and the pairing gap Δ. The peak widths are indicated by double arrows in Fig. 9 as similarly defined in Appendix D. Both the peak intensity and the peak width are plotted as a function of temperature in Fig. 9(b). Evidently, by increasing temperatures, the peak width gets broadened, while the peak intensity is reduced.

APPENDIX F: EVIDENCE FOR A TRANSPARENT INTERFACE BETWEEN TOPOLOGICAL INSULATOR AND SUPERCONDUCTOR

In this section, we demonstrate by our numerical simulations that the topological insulator/superconductor (TI/SC) interface in our transport measurements is very transparent. In particular, we show that by reducing the interfacial transparency, both features of flat bias-independent conductance plateau (BICP) and pronounced zero-bias conductance peak (ZBCP) differ qualitatively from the experimental results.

Both the surface states and the bulk states are properties of the topological insulator. Tuning the coupling strength t_c between the bottom layer of the topological insulator and the top layer of the superconductor controls the transparency of the interface. By reducing the interfacial coupling strength t_c, which effectively reduces the interfacial transparency, the superconducting proximity effects on both the topological surface states and the bulk states in the TI become less effective. As a result (Fig. 10), the flat BICP due to superconducting TSS evolves into a broad conductance peak, and the intensity of the pronounced ZBCP due to the bulk states is also suppressed. In other words, a well-defined BICP can be seen only when the interface is very transparent (for example, when the hopping t_c between the TI and the superconductor is almost the same as the hopping t in the superconductor).

APPENDIX G: ESTIMATION OF THE THOULESS ENERGY OF THE BULK STATES OF Bi_2Se_3

(i) For bulk states of Bi_2Se_3 flakes

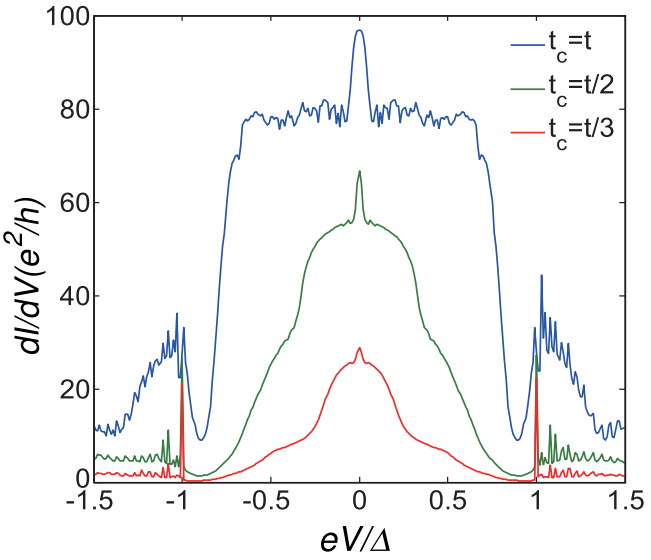

FIG. 10. Zero-temperature dI/dV spectra at different t_c, where t_c is the coupling strength. Due to reduced interfacial transparency, the proximity effects in both the surface states and the bulk states become less effective. As a result, the original bias-independent conductance plateau shrinks into a broad conductance peak, and the intensity of the original zero-bias peak is also reduced.

The diffusion constant in 3D bulk states should be [56]

$$D = \tfrac{1}{3} v_F l_s = \tfrac{1}{3} v_F (v_F \tau), \tag{G1}$$

where v_F is the Fermi velocity, l_s is the mean free path, and τ is the diffusion time. The Fermi velocity of the bulk states can be calculated by

$$v_F = \frac{\hbar k_F}{m^*}, \tag{G2}$$

where $\hbar$ is the reduced Planck constant, the $k_F = (3\pi^2 n_{3D})^{\frac{1}{3}}$ is the Fermi wave vector with n_{3D} as the carrier density of the 3D bulk states of Bi_2Se_3, and m^* is the effective mass of the electrons in the bulk states, which roughly equals to the standard electron mass. The diffusion time τ is calculated by

$$\tau = \frac{\mu m^*}{e}, \tag{G3}$$

where μ is the mobility, and e is the elementary charge. The carrier density n_{3D} is about $2.27 \times 10^{19}/\mathrm{cm}^3$ calculated from the Hall measurements on our Bi_2Se_3 flakes, and the mobility is estimated to be about $0.034\ \mathrm{m}^2/\mathrm{Vs}$. Combining all the equations and parameters together, we arrive at

$$E_{th} = \frac{\hbar D}{L^2} = \frac{1}{3}\frac{\hbar^3 \mu}{m^* e L^2}(3\pi^2 n_{3D})^{\frac{2}{3}} \sim 0.036\ \mathrm{meV} \tag{G4}$$

$$L_{th} = \sqrt{\hbar D/(2\pi k_B T)} \sim 28\ \mathrm{nm}/\sqrt{T}. \tag{G5}$$

The distance L in Eq. (G4) should be the thickness of the Bi_2Se_3 layer as our $NbSe_2/Bi_2Se_3$ hybrid structure is vertically aligned, as indicated in Figs. 1(a) and 4(a) in the main text. It can be seen that the Thouless energy of the bulk states is about 0.036 meV, which is close to the ZBCP width we measured from the dI/dV spectra in Fig. 3(a).

(ii) For topological surface states of Bi_2Se_3 flakes

Based on the measured magnetoresistance properties of Bi_2Se_3 flake in Appendix B, the Fermi velocity v_F and the length of mean free path l_s is 5.92×10^7 cm/s and 28.2 nm, respectively, for the topological surface states of Bi_2Se_3 flake. However, as the surface states are localized at the interface, the distance L cannot be identified readily to be the thickness of the Bi_2Se_3 in our heterostructures.

[1] E. Majorana, Nuovo Cimento **14**, 171 (1937) [L. Maiani, Soryushiron Kenkyu (Engl. transl.) **63**, 149 (1981)].
[2] N. Read and D. Green, Phys. Rev. B **61**, 10267 (2000).
[3] D. A. Ivanov, Phys. Rev. Lett. **86**, 268 (2001).
[4] L. P. Rokhinson, X. Y. Liu, and J. K. Furdyna, Nat. Phys. **8**, 795 (2012).
[5] A. Das, Y. Ronen, Y. Most, Y. Oreg, M. Heiblumand, and H. Shtrikman, Nat. Phys. **8**, 887 (2012).
[6] M. T. Deng, C. L. Yu, G. Y. Huang, M. Larsson, P. Caroff, and H. Q. Xu, Nano Lett. **12**, 6414 (2012).
[7] V. Mourik, K. Zuo, S. M. Frolov, S. R. Plissard, E. P. A. M. Bakkers, and L. P. Kouwenhoven, Science **336**, 1003 (2012).
[8] A. D. K. Finck, D. J. Van Harlingen, P. K. Mohseni, K. Jung, and X. Li, Phys. Rev. Lett. **110**, 126406 (2013).
[9] H.-H. Sun, K.-W. Zhang, L.-H. Hu, C. Li, G.-Y. Wang, H.-Y. Ma, Z.-A. Xu, C.-L. Gao, D.-D. Guan, Y.-Y. Li, C. Liu, D. Qian, Y. Zhou, L. Fu, S.-C. Li, F.-C. Zhang, and J.-F. Jia, Phys. Rev. Lett. **116**, 257003 (2016).
[10] L. Fu and C. L. Kane, Phys. Rev. Lett. **100**, 096407 (2008).
[11] L. Fu and C. L. Kane, Phys. Rev. Lett. **102**, 216403 (2009).
[12] K. T. Law, P. A. Lee, and T. K. Ng, Phys. Rev. Lett. **103**, 237001 (2009).
[13] X.-L. Qi and S.-C. Zhang, Rev. Mod. Phys. **83**, 1057 (2011).
[14] A. C. Potter and L. Fu, Phys. Rev. B **88**, 121109 (2013).
[15] D. Zhang, J. Wang, A. M. DaSilva, J. S. Lee, H. R. Gutierrez, M. H. W. Chan, J. Jain, and N. Samarth, Phys. Rev. B **84**, 165120 (2011).
[16] J. R. Williams, A. J. Bestwick, P. Gallagher, S. S. Hong, Y. Cui, A. S. Bleich, J. G. Analytis, I. R. Fisher, and D. Goldhaber-Gordon, Phys. Rev. Lett. **109**, 056803 (2012).
[17] M. Veldhorst, M. Snelder, M. Hoek, T. Gang, X. L. Wang, V. K. Guduru, U. Zeitler, W. G. van der Wiel, A. A. Golubov, H. Hilgenkamp, and A. Brinkman, Nat. Mater. **11**, 417 (2012).
[18] H.-C. Liu, H.-T. He, B.-K. Li, S.-G. Liu, Q. L. He, G. Wang, I.-K. Sou, and J. N. Wang, Appl. Phys. Lett. **103**, 152601 (2013).
[19] P. Zareapour, A. Hayat, S. Y. F. Zhao, M. Kreshchuk, A. Jain, D. C. Kwok, N. Lee, S.-W. Cheong, Z. Xu, A. Yang, G. D. Gu, S. Jia, R. J. Cava, and K. S. Burch, Nat. Commun. **3**, 1056 (2012).

[20] F. Yang, Y. Ding, F. Qu, J. Shen, J. Chen, Z. Wei, Z. Ji, G. Liu, J. Fan, C. Yang, T. Xiang, and L. Lu, Phys. Rev. B **85**, 104508 (2012).
[21] Y. Xu, I. Miotkowski, C. Liu, J. Tian, H. Nam, N. Alidoust, J. Hu, C.-K. Shih, M. Z. Hasan, and Y. P. Chen, Nat. Phys. **10**, 956 (2014).
[22] T. Yilmaz, I. Pletikosic, A. P. Weber, J. T. Sadowski, G. D. Gu, A. N. Caruso, B. Sinkovic, and T. Valla, Phys. Rev. Lett. **113**, 067003 (2014).
[23] S.-Y. Xu, C. Liu, A. Richardella, I. Belopolski, N. Alidoust, M. Neupane, G. Bian, N. Samarth, and M. Z. Hasan, Phys. Rev. B **90**, 085128 (2014).
[24] C.-G. Andres, B. Michele, M. Rianda, S. Vibhor, J. Laurens, S. J. van der Z. Herre, and A. S. Gary, 2D Mater. **1**, 011002 (2014).
[25] T. Yokoya, T. Kiss, A. Chainani, S. Shin, M. Nohara, and H. Takagi, Science **294**, 2518 (2001).
[26] D. J. Rahn, S. Hellmann, M. Kallane, C. Sohrt, T. K. Kim, L. Kipp, and K. Rossnagel, Phys. Rev. B **85**, 224532 (2012).
[27] G. E. Blonder, M. Tinkham, and T. M. Klapwijk, Phys. Rev. B **25**, 4515 (1982).
[28] S. Kashiwaya, Y. Tanaka, M. Koyanagi, and K. Kajimura, Phys. Rev. B **53**, 2667 (1996).
[29] T. M. Klapwijk, J. Supercond. **17**, 593 (2004).
[30] Y. Xia, D. Qian, D. Hsieh, L. Wray, A. Pall, H. Lin, A. Bansil, D. Grauer, Y. S. Hor, R. J. Cava, and M. Z. Hasan, Nat. Phys. **5**, 398 (2009).
[31] M. Petrushevsky, E. Lahoud, A. Ron, E. Maniv, I. Diamant, I. Neder, S. Wiedmann, V. K. Guduru, F. Chiappini, U. Zeitler, J. C. Maan, K. Chashka, A. Kanigel, and Y. Dagan, Phys. Rev. B **86**, 045131 (2012).
[32] B. Pannetier and H. Courtois, J. Low. Temp. Phys. **118**, 599 (2000).
[33] Y. de Wilde, T. M. Klapwijk, A. G. M. Jansen, J. Heil, and P. Wyder, Physica B **218**, 165 (1996).
[34] S.-Y. Xu, N. Alidoust, I. Belopolski, A. Richardella, C. Liu, M. Neupane, G. Bian, S.-H. Huang, R. Sankar, C. Fang, B. Dellabetta, W. Dai, Q. Li, M. J. Gilbert, F. Chou, N. Samarth, and M. Z. Hasan, Nat. Phys. **10**, 943 (2014).
[35] B. J. van Wees, P. de Vries, P. Magnee, and T. M. Klapwijk, Phys. Rev. Lett. **69**, 510 (1992).
[36] P. Xiong, G. Xiao, and R. B. Laibowitz, Phys. Rev. Lett. **71**, 1907 (1993).
[37] Z. D. Kvon, T. I. Baturina, R. A. Donaton, M. R. Baklanov, K. Maex, E. B. Olshanetsky, A. E. Plotnikov, and J. C. Portal, Phys. Rev. B **61**, 11340 (2000).
[38] F. Yang, F. Qu, J. Shen, Y. Ding, J. Chen, Z. Ji, G. Liu, J. Fan, C. Yang, L. Fu, and L. Lu, Phys. Rev. B **86**, 134504 (2012).
[39] A. Kastalsky, A. W. Kleinsasser, L. H. Greene, R. Bhat, F. P. Milliken, and J. P. Harbison, Phys. Rev. Lett. **67**, 3026 (1991).
[40] C. Nguyen, H. Kroemer, and E. L. Hu, Phys. Rev. Lett. **69**, 2847 (1992).
[41] G. Koren, Supercond. Sci. Tech. **28**, 025003 (2015).
[42] F. Laube, G. Goll, H. v. Lhneysen, M. Fogelstrm, and F. Lichtenberg, Phys. Rev. Lett. **84**, 1595 (2000).
[43] S. Kashiwaya, Y. Tanaka, M. Koyanagi, H. Takashima, and K. Kajimura, Phys. Rev. B **51**, 1350 (1995).
[44] C. K. Chiu, M. J. Gilbert, and T. L. Hughes, Phys. Rev. B **84**, 144507 (2011).
[45] J. M. Rowell, A. G. Chynoweth, and J. C. Phillips, Phys. Rev. Lett. **9**, 59 (1962).
[46] M. Jourdan, M. Huth, and H. Adrian, Nature (London) **398**, 47 (1999).
[47] H. Courtois, Ph. Gandit, D. Mailly, and B. Pannetier, Phys. Rev. Lett. **76**, 130 (1996).
[48] P. Charlat, H. Courtois, Ph. Gandit, D. Mailly, A. F. Volkov, and B. Pannetier, Phys. Rev. Lett. **77**, 4950 (1996).
[49] A. Llords, A. Palau, J. Gzquez, M. Coll, R. Vlad, A. Pomar, J. Arbiol, R. Guzmn, S. Ye, V. Rouco, F. Sandiumenge, S. Ricart, T. Puig, M. Varela, D. Chateigner, J. Vanacken, J. Gutirrez, V. Moshchalkov, G. Deutscher, C. Magen, and X. Obradors, Nat. Mater. **11**, 329 (2012).
[50] S. Foner and E. J. McNiff Jr., Phys. Lett. A **45**, 429 (1973).
[51] H.-C. Liu, S. Liu, Y. Yi, H. He, and J. N. Wang, 2D Mater. **2**, 045002 (2015).
[52] H. Zhang, C.-X. Liu, X.-L. Qi, X. Dai, Z. Fang, and S.-C. Zhang, Nat. Phys. **5**, 438 (2009).
[53] K. Ebihara, K. Yada, A. Yamakage, and Y. Tanaka, Physica E **44**, 885 (2012).
[54] D. S. Fisher and P. A. Lee, Phys. Rev. B **23**, 6851 (1981).
[55] M. P. Anantram and S. Datta, Phys. Rev. B **53**, 16390 (1996).
[56] H.-Z. Lu and S.-Q. Shen, Phys. Rev. B **92**, 035203 (2015).